UWB Bowtie Antenna for Medical Microwave Imaging Applications

Ondrej Fiser, *Member, IEEE*, Vojtech Hruby, Jan Vrba, *Life Member, IEEE*, Tomas Drizdal, Jan Tesarik, Jan Vrba, Jr., and David Vrba, *Member, IEEE*

Abstract— This work presents a design and experimental validation of a compact ultrawideband (UWB) bowtie antenna and balanced-to-unbalanced (balun) circuit for medical microwave imaging (MWI) applications working in the frequency band of 1–6 GHz. The UWB balun is perpendicularly attached to the planar bowtie arms, whose dimensions were miniaturized by rounding the bowtie edges. The antenna reflection coefficient was lower than -12 dB for tissues with a higher water content. The antenna possesses a high radiation efficiency (over 80%) and very low backward radiation. The predicted and measured specific absorption rate (SAR) distributions together with the electric field $|E|$ distribution proved a symmetrical radiation pattern. The potential of the presented antenna element was demonstrated by successful reconstruction of the images from the measured data by MWI methods. For this purpose, an MWI system equipped with eight antennas was implemented. The radar approach was used to determine the region of interest (ROI) where the area for microwave tomography reconstruction was identified. The dielectric properties within the ROI were reconstructed by using the Born approximation method at 1 GHz. This confirmed that the antenna can be used as the basis for more accurate multifrequency MWI systems and can be implemented in UWB MWI hybrid systems.

Index Terms— Microwave imaging (MWI), ultrawideband (UWB) radar, UWB antenna.

I. INTRODUCTION

MICROWAVE imaging (MWI) methods in medicine have been explored intensively in the last two decades as an alternative to current conventional imaging methods, such as magnetic resonance imaging (MRI), computed tomography (CT), and positron emission tomography (PET) [1]. The advantage of MWI methods is its relatively short acquisition time and operating costs [2]. Furthermore, MWI utilizes nonionizing radiation and its systems can be implemented in a small and compact way [3]. MWI has the potential to be effectively applied directly in ambulance vehicles in the diagnosis of brain stroke, resulting in a significant reduction in the time between the onset of the stroke and its treatment. This is the key aspect to eliminate negative health consequences and obtain a better patient prognosis. Another possible application of MWI systems is noninvasive temperature monitoring during hyperthermia treatment in which the temperature of the target tumor region is artificially increased to the range of 40 °C–44 °C for at least one hour [4]. This temperature increase can be detected as a function of changes in dielectric properties using the MWI technique. The MWI methods are based on the exposure of the imaging domain with electromagnetic (EM) waves and the measurement of reflected and scattered EM waves at interfaces with different dielectric properties usually using antenna arrays. The region of interest (ROI) can be scanned and visualized in 3-D through various reconstruction algorithms (depending on the MWI method) processing information about EM waves received by individual antenna elements. Such 3-D reconstructions are reported in [5] and [6]. The image reconstruction capability of the MWI system is greatly influenced by the characteristics of the antenna elements we used.

The selection of an appropriate antenna element for MWI system depends on the selected mode of MWI. First, the microwave tomography (MT) method uses signal processing in the frequency domain and applies methods capable of estimating the dielectric profile of the scanned region. The antennas of MT systems are usually placed equidistantly around the imaging domain [5]–[10]. Second, radar-based (confocal) imaging methods process signals in the time domain and can locate dielectric inhomogeneity (scatterers) within a tissue, without the ability to reconstruct the dielectric profile. Radar-based reconstruction algorithms are usually significantly less demanding on computation and time. The basic principle is to transmit ultrawideband (UWB) signals, providing high imaging resolution. The transmitted signal can be formed by short periodically repeated pulses, pseudorandom binary sequences, and so on. Such radar-based systems for biomedical imaging are presented in [11]–[13]. By combining these two principles, i.e., the MT and radar-based approach, it brings the possibility to reduce the analyzed tissue area to the less voluminous region containing significant inhomogeneity. Reduction of the imaged area can effectively speed up the MWI reconstruction [14], [15]. These novel combined

TABLE I
COMPARISON OF THE ANTENNA SPECIFICATIONS
WITH HERE PRESENTED ANTENNA

Ref.	Usage	General dimensions [W x L x h] (mm³)	Freq. band (GHz)	BW (%)
[23]	Medical imaging	30 x 30 x 1.27	0.5-2	120
[24]	Head imaging	68 x 68 x 12	1-1.7	63
[25]	Head imaging	25 x 28 x 5.6	1-4.3	120
[26]	Bone imaging	45 x 40 x 0.5	1.2-4.1	109
[27]	Head imaging	50 x 50 x 70	0.8-1.2	40
[28]	Head imaging	20 x 20 x 8.3	0.5-5	163
Presented antenna	Medical imaging	60 x 60 x 50	1-6	143

MWI systems lead to new requirements for the antenna elements. Among UWB antennas that are suitable for MWI at microwave frequencies are Vivaldi planar antennas [15], [16], double ridged horn antennas [17], [18], planar monopoles [6], [19], [20], and bowtie dipoles [21], [22].

The planar Vivaldi antenna proposed by Bourqui *et al.* [16] uses exponentially tapered antipodal arms to radiate energy directly to the tissue. This antenna was designed for the breast cancer detection system based on the radar approach. Due to the very low relative permittivity of the breast (approximately $\varepsilon_r = 6$), canola oil is used as a matching liquid. UWB ridged horn antennas have high radiation efficiency, and the backward and side radiation is suppressed. These ridged horn antennas are usually filled with high permittivity material (e.g., ceramics [18]) inserted inside the antenna and reducing the antenna dimensions. The weight of the antenna is high and, due to its filling, is also difficult to manufacture compared with other eligible antennas for MWI. Planar UWB monopole antennas, for example, from Jafari *et al.* [19] offer a low-cost solution of the problem, as they are easy to fabricate. Planar monopoles do not need a matching liquid because they can be placed on the surface of the analyzed tissue. However, the advantage of the simplicity of planar design entails the drawback of power supply in the plane of the monopole patch, which is not very appropriate and makes the use of such a monopole in an array difficult from the array perspective. Furthermore, the radiation pattern of the planar UWB monopoles varies quite significantly with frequency [20], which may cause distortion in the time domain. Bowtie dipoles, generally planar dipoles and its modifications, are simple to fabricate. The geometry is broadband and the antenna is fully attachable directly to the tissue (the matching liquid is not needed). Compared with the horn and Vivaldi antennas, the bowtie antenna has a lower radiation effectivity and is more sensitive to the surrounding environment. Due to the high permittivity value of the muscle tissue, a higher part of the EM energy is emitted toward the phantom, which improves the efficiency. However, the bowtie antenna requires symmetrical feeding, which is usually suitable only for a limited frequency range. Table I compares UWB antennas for MWI devices with here mentioned UWB antenna.

The purpose of this work was to design an UWB bowtie antenna including UWB balanced-to-unbalanced (balun) for combined MT. In the first step, we have studied and compared several possible microstrip UWB baluns (Sections II-A and II-B). The most promising balun was combined with the bowtie antenna, whose dimensions were minimized by adjusting the shape of bowtie edges using a numerical parametric study. In the next step, we numerically tested basic antenna parameters for antenna usability. We numerically tested antenna radiation efficiency and verified that bowties arms are symmetrically fed by visualization of surface current density and $|E|$ field distribution. The sensitivity of the antenna to air gaps formation and the signal distortion of the UWB signal were tested (Section II-A3). We compared the predicted and measured reflection characteristics and specific absorption rate (SAR) distribution of manufactured UWB bowtie antenna at the phantom of different equivalent tissues (Section II-A4). Then, we equidistantly positioned eight manufactured UWB bowtie antennas into the MWI head system. The potential of this system to detect and reconstruct the dielectric inhomogeneity inside the human head phantom using a combination of radar and MT approaches was studied (Section III).

II. ANTENNA DESIGN

The antenna presented in this article is intended for the biomedical MWI applications. MWI systems are mostly composed of an array of antennas that are attached to the area to be imaged. The antenna parameters influence the reconstruction/imaging ability of the entire system. The antenna used in UWB MWI system should satisfy multiple demands in the intended ultrawide frequency band, which are as follows.

1) Efficient transmission of EM energy into the tissue—low reflection coefficient of the antenna, minimized radiation to the surrounding regions.
2) Adequate near-field radiation patterns—wide beamwidth in the azimuth plane and acceptably narrow beamwidth in the elevation plane.
3) Minimal (time domain) distortion of the transmitted/received signals and short impulse response to achieve high spatial resolution of the system.
4) Acceptable physical dimensions of the antenna element. The dimensions of the antenna determine the maximum number of antennas that could be distributed around the area to be imaged. According to our experience, the minimal number of antennas for successful MWI of, i.e., head with decent accuracy in 2-D is 8 (in single ring arrangement). We estimate that up to 16 bowtie antennas can be positioned to cover the entire head area (in 3-D).

A. Methods—Antenna Design

In the first step of the UWB bowtie antenna development, we designed the bowtie arms shape. Then, we created UWB microstrip balun, as a bowtie dipole is a symmetrical structure, and requires balanced feeding. In the third step, we optimized the entire UWB bowtie antenna geometry to fulfill given performance requirements. The commercial EM numerical
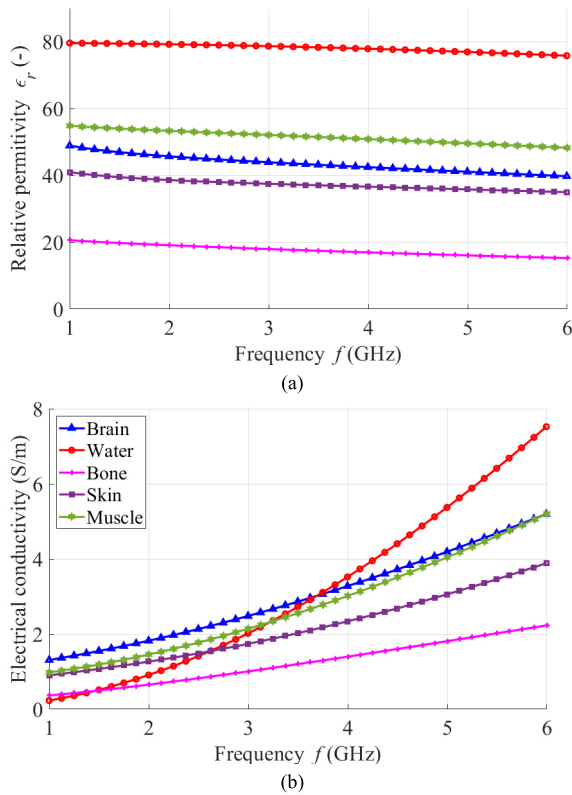
Fig. 1. Dielectric parameters of considered biological tissues: (a) relative permittivity and (b) electrical conductivity of tissues used in simulations in the frequency band of 1–6 GHz. Parameters were imported from [29].
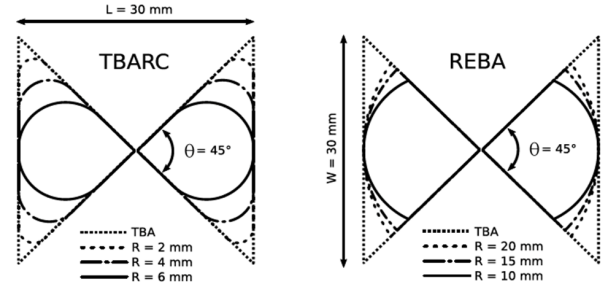

Fig. 2. Tested bowtie arms geometries: TBARC and REBA with different rounding radius R derived from the fundamental TBA geometry.

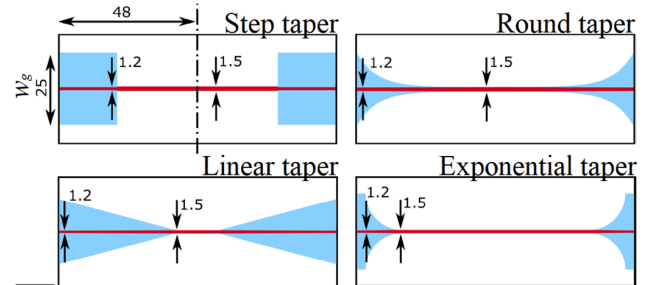Fig. 3. Transition geometries with different shapes of ground transition (blue)—dimensions are presented in millimeters.

simulator COMSOL Multiphysics (COMSOL AB, Stockholm, Sweden) based on the finite-element method (FEM) and Sim4life (Speag, Zürich, Switzerland) based on the finite difference time domain (FDTD) method were used for the antenna design and parameters optimization. In all numerical simulations, the antenna was directly attached to the homogeneous phantom with dielectric parameters being similar to the specific human tissues (see Fig. 1). Fig. 1 shows used relative permittivity and electrical conductivity of considered tissues in the whole simulated band, and data were adopted from [29].

1) Bowtie Antenna Arms: A bowtie antenna is a planar structure usually designed as a one-layer PCB. We have considered several eligible shapes of bowtie arms available in the literature [30]. We tested the following geometries, namely, "rounded bowtie antenna" (REBA), "triangle bowtie antenna with rounded corners" (TBARC), and fundamental "triangle bowtie antenna" (TBA) (see Fig. 2).

All shapes were derived from the TBA geometry with total length and width of 30 mm. Bowtie arms were placed at 1.524 mm height substrate with dielectric properties corresponding to the Rogers RO4003C (Rogers Corporation, Chandler, AZ, USA). In the simulated antenna, the angle θ was fixed to 45° as awhole antenna structure together with balun showed the best reflection coefficient. The bowtie antenna performance is also dependent on the dipole rounding radius R. The parametric study has been carried out to optimize the impedance matching of the proposed antenna over frequency band of interest.

2) UWB Balun: UWB balun symmetrization circuit is a key feature in the design of UWB antenna with symmetrical radiating pattern. The most applicable UWB balun solutions are ferrite or planar-tapered baluns. We decided to use the planar-tapered UWB balun over ferrite baluns. This decision was based on assumption that the ferrites baluns can transform only limited RF power.

According to our experience, the planar-tapered UWB baluns also cause lower UWB signal distortion at higher frequencies in comparison with the ferrite baluns.

We calculated the strip widths of microstrip line and double-sided parallel strip line (DSPSL) in a way to obtain 50 Ω impedance at used 0.508 mm height Rogers RO4003C substrate. The impedance characteristic was calculated according to the formulas presented in [31]. The balun length was set to 48 mm as a quarter of wavelength at 1 GHz. The width of the microstrip ground plane was set to $w_g = 25$ mm. Four different balun shapes were considered, and the corresponding numerical models were created. The baluns were modeled as mirrored pairs with microstrip line at both ends and the DSPSL in the middle (in total 2×48 mm^2 long). Geometries of the baluns are shown in Fig. 3. For all balun versions, S-parameters were calculated in the frequency band of 0.2–6 GHz. The antenna for the medical MWI should be directly attachable to the imaged area. If this option is to be maintained, then it is convenient to feed the bowtie dipole in a direction perpendicular to the plane of the dipole arms. The balun was attached perpendicularly to the bowtie dipole arms (TBARC with a radius of 6 mm).

3) Simulation of Antenna Properties: The following experiments were designed to clarify UWB antenna parameters, such as antenna usability for MWI of different tissues, antenna sensitivity to lower phantom contact to tissue, antenna radiation efficiency, and antenna radiation symmetry. These experiments were performed in the environment of COMSOL Multiphysics

(FEM-based) as numerical simulations and in the Sim4life numerical simulator (FDTD-based). First, a simple numerical model consists of a UWB antenna surrounded by a sphere of a radius of 20 cm where the front hemisphere was defined as the brain phantom. To acquire further insight into antenna performance, we have studied the current distribution over the surface of the bowtie arms. The current distribution was visualized using vectors to prove the ability of the balun to provide sufficient symmetric feeding of the bowtie arms. Second, we evaluated the radiation efficiency of the antenna. The introduced antenna is intended to operate in a lossy medium (average human brain phantom) in the near-field antenna region. To express the antenna radiation efficiency to the human brain phantom, the parameter E_f was introduced. The parameter E_f was calculated according to the following equation:

$$E_f = \frac{P_{head}}{P_{input}} \cdot 100(\%) \tag{1}$$

where P_{input} (W) is the input power, and P_{head} (W) is the power absorbed in the brain phantom in front of the antenna. The method of radiation patterns, with respect to antenna theory [32], [33], is (for this case) hardly applicable for the estimation of radiation efficiency. Instead, we proposed to evaluate SAR (W/kg) in yz plane for frequency range 1–6 GHz with a 2 GHz step. The numerically obtained SAR was normalized by the maximum value and compared with the measured SAR. The boundary conditions of the model were set to scattering boundary conditions that suppress reflections.

We further numerically evaluated the normalized magnitude of the intensity of the electric field intensity $|E|$ depending on the radiation angle (°) in xz and yz planes (H- and E-planes). The electric field intensity was computed for the frequencies 1, 3, and 5 GHz in both planes perpendicular to the antenna (Fig. 4(a)—red curve is for E-plane and green curve for H-plane). The evaluation angle ranged from $-90°$ to $90°$ with respect to the antenna position. The transition between brain and air hemisphere stands for 0° angle.

Furthermore, the antenna medical versatility was verified numerically and experimentally via the comparison of the reflection parameters following the setup in Fig. 5. In this setup, the whole antenna, including the SMA model, UWB balun, and dipole arms, is faced with a single tissue cubic phantom. The numerical analysis is performed in the Sim4Life software as the phantom mimics the brain, bone, skin, and muscle dielectric properties (relative permittivity and electrical conductivity—presented in Fig. 1) [29].

The antenna ability to transmit and receive an UWB signals with low distortion was tested using the same simulation setup described above (see Fig. 5). The UWB signal that is emitted and which is propagating through lossy media (i.e., human tissues) is attenuated. This attenuation is frequency dependent and affects the signal amplitude and signal shape. To eliminate this effect, and only for this signal distortion study, the phantom electrical conductivity was set to 0 (S/m). Thus, we can observe just signal distortion caused by antenna element itself. One antenna was determined as transmitting (T_x) one. It emits the UWB Gaussian pulse of
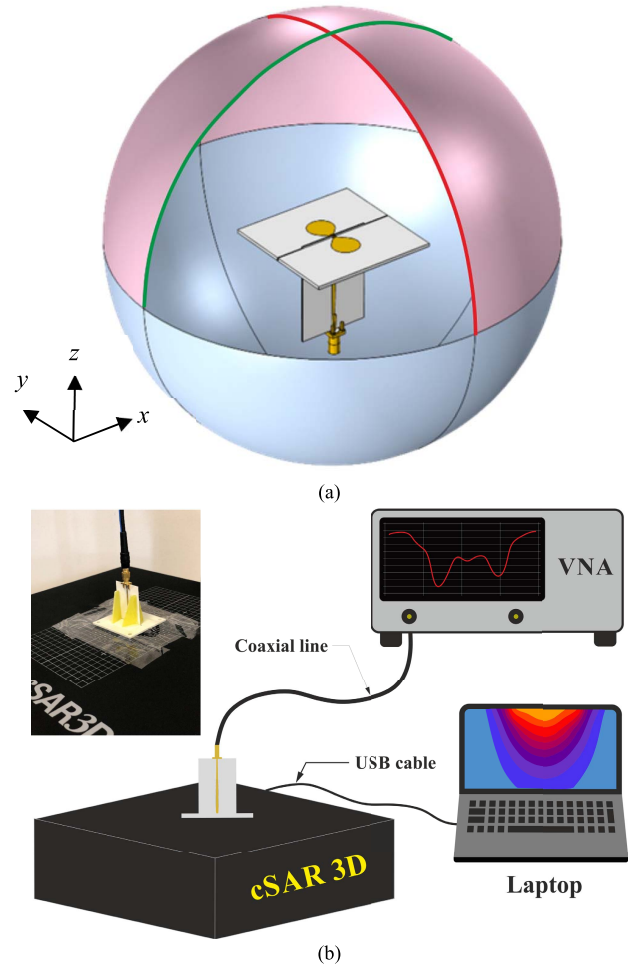

(a)

(b)

Fig. 4. (a) Numerical model for calculation of antenna power efficiency and SAR simulation and (b) SAR measurement setup.
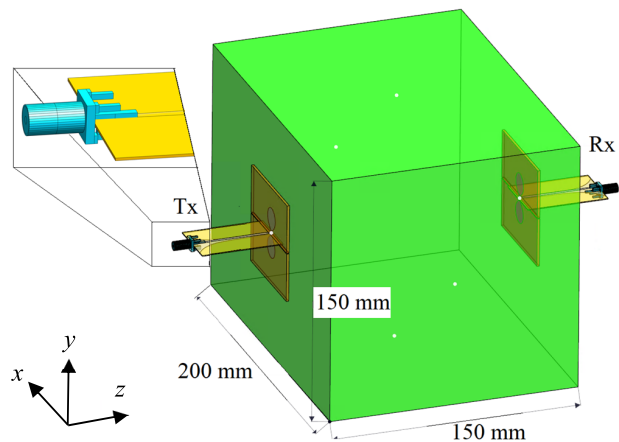

Fig. 5. Numerical model used to optimize antenna dimensions and to calculate the reflection coefficient for different phantom configurations and antenna signal distortion. A detail of the antenna feeding is displayed in the top left corner.

the frequency band of 1–6 GHz. The opposite antenna was in the receiving mode (R_x). This analysis was done using the Sim4Life software (ZMT Zurich Med Tech AG, Zürich). The most common parameter for UWB signal distortion evaluation is fidelity, which is calculated as a cross correlation between
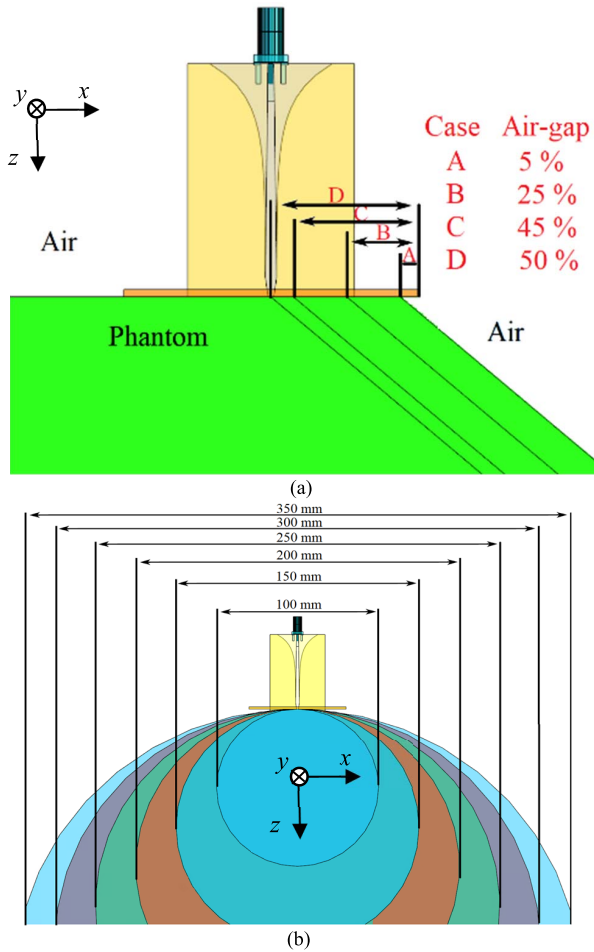
(a)

(b)

Fig. 6. Simulation study of lower antenna contact between: (a) flat phantom, where the green trimmed cube is representing brain phantom. Lower antenna contact to: (b) rounded phantom of various diameters between 100 and 350 mm.

the normalized T_x and R_x signals. The fidelity factor F (-) is defined as follows [36]:

$$F = max \frac{\int_{-\infty}^{+\infty} T(t)R(t+\tau)dt}{\sqrt{\int_{-\infty}^{+\infty} |T(t)^2|dt \int_{-\infty}^{+\infty} |R(t)^2|dt}} \quad (2)$$

where $T(t)$ is transmitted signal, $R(t)$ is received signal, t is time, and τ is time displacement. The time domain signals from the proposed antenna are also compared with signals from previously used UWB bowtie antenna (for brain imaging) as well as the fidelity factor F.

Subsequently, there are two additional numerical studies of the antenna sensitivity to the lower phantom contact (partial air gaps at the antenna edges formations which can occur in real applications): 1) on flat [Fig. 6(a)] and 2) rounded phantom [Fig. 6(b)] were performed. The dielectric parameters of the phantom were set as human brain (see the dielectric parameters in Fig. 1). First, we tested four cases of reduced contact between antenna and flat brain phantom. The ratio of contact with phantom and air for different cases is listed in the following Table II and is visualized in Fig. 6(a)—case A. In all simulated cases, the part of the phantom under the antenna was cut off and replaced by air (situations A–D). We observed

Case	Antenna/Phantom contact	Air gap
A	95 %	5 %
B	75 %	25 %
C	55 %	45 %
D	50 %	50 %

the influence of the partial contact on $|S_{11}|$ parameter of the antenna. In the second experiment, the phantom was attached to the series of rounded brain phantoms of different diameter [see Fig. 6(b)]. Generally, we tested six phantoms of diameters from 100 to 350 mm with 50 mm step. This should represent a real clinical situation when the antenna will be attached to the rounded part of the body (i.e., head, arm, leg, etc.).

4) Measurement of Antenna Properties: The SAR in the brain phantom was measured by certified cSAR3D (Schmidt & Partner Engineering AG, Zürich) [34], which is containing the flat head phantom (head tissue simulating medium—HSL) setup together with vector network analyzer (VNA) ZNB8-32 (Rohde & Schwarz, Munich, Germany) used as a microwave signal generator [see diagram of setup in Fig. 4(b)]. The dielectric properties of the HSL phantom are as human head ±10% [34]. The dielectric properties are identical as presented in Fig. 1 for brain tissue. The output power of the VNA was set to 13 dBm. The antenna was directly attached to the center of the cSAR3D phantom. Good adhesion of the antenna to the phantom was achieved by applying a very thin water layer to avoid air gaps creation.

For the measurement of the antenna $|S_{11}|$ parameter, the fabricated dipole antenna was placed directly in contact with the phantom. The head phantom preparation is further described in Section III-A. The agar muscle phantom was prepared according to the recipe presented in [35]. The VNA R&S FSH8 (Rohde & Schwarz) was used for reflection coefficient measurements in the band 0.5–6 GHz.

B. Simulation Results—Antenna Design

1) Simulation of Bowtie Antenna Arms: The results of the simulation of mentioned geometries in the frequency band of 0.5–6 GHz are presented in Fig. 7(a) and (b). Obtained $|S_{11}|$ curves showed that TBA shapes are better impedance matched at lower frequencies, but all simulated shapes have sufficient reflection coefficient ($|S_{11}|$ lower than −10 dB). Due to the demands on the compact antenna size in the imaging system, the TBARC geometry with a rounding radius of 6 mm was chosen for the proposed antenna, as this geometry enables the reduction of the bowtie arms width from 30 mm in the TBA geometry to only 13 mm and offers the lowest predicted reflection coefficient from all studied shapes.

2) Simulation of UWB Balun: S-parameters (modules of S_{11} and S_{21}) of all four tested baluns were numerically calculated and are presented in Fig. 8. Best results were obtained with the exponential tapered balun, which was adopted from [16]. The balun geometry was modified to achieve better reflection
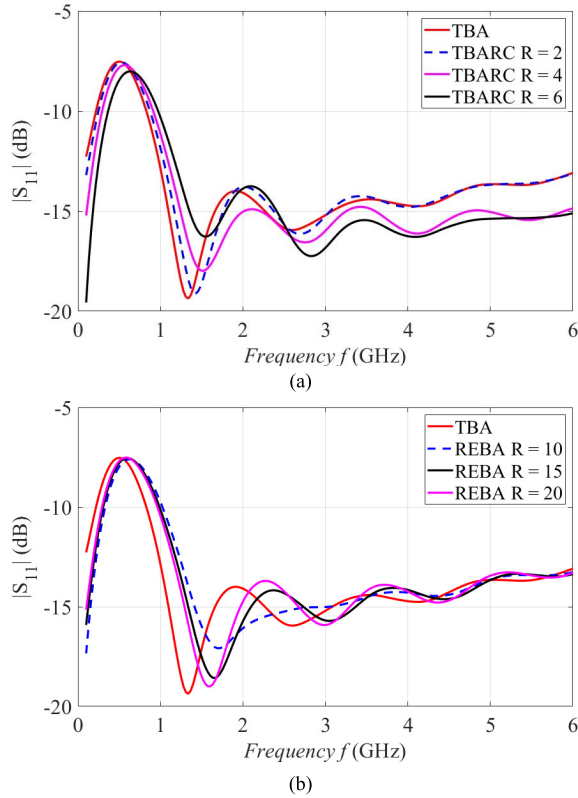
Fig. 7. Simulated $|S_{11}|$ for: (a) TBARC and (b) REBA geometry of different radius R.
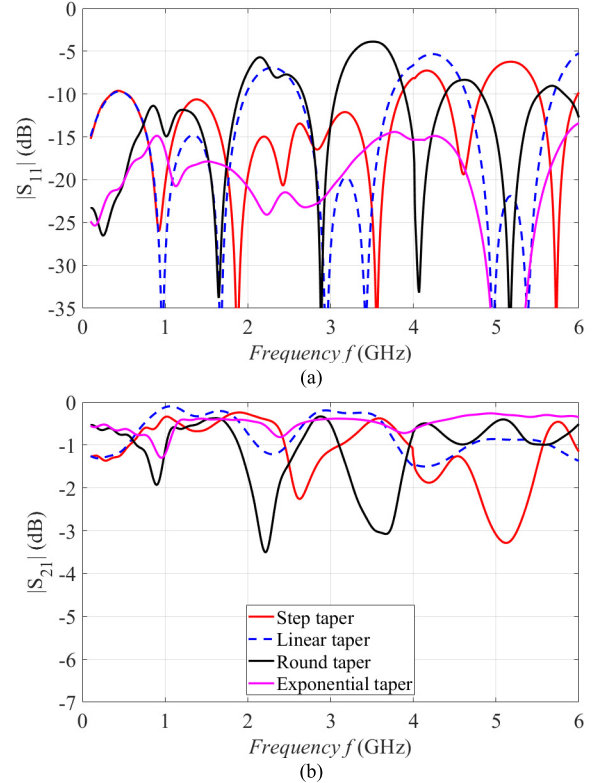

Fig. 8. Simulated module of: (a) reflection coefficient ($|S_{11}|$) and (b) transmission coefficient ($|S_{21}|$) of baluns of different ground transition shapes (geometries are presented in Fig. 2).

coefficient within used frequency band. The modified parameters were $W_{DL} = 2.3$ mm and $L_p = 4.5$ mm. All results were calculated for the width of the microstrip ground plane $W_g = 25$ mm (see Fig. 3). The influence of small variations of the microstrip ground plane width w_g on balun performance was found to be insignificant. The optimized and finalized balun geometry with dimensions is presented in Fig. 9. The exponential balun offers the highest and frequency stable transmission coefficient together with the lowest reflection coefficient.

3) Finalized Antenna Dimensions: The finalized geometry of the designed UWB bowtie antenna with inserted balun between the bowtie arms is optimized for operation in the frequency bandwidth of 1–6 GHz. The resulted antenna model is shown in Fig. 10. The antenna is of compact size ($60 \times 60 \times 50$ mm^3) with the possibility of further dimension reduction, as the conductive bowtie arms motive was minimized as described earlier.

4) Simulation of Finalized Antenna Properties: The surface current density J (A/m) distribution in the indicated frequency bandwidth on the bowtie arms of UWB antenna is shown in Fig. 11. The module of surface current density $|J|$ is represented by color map. The white cones are representing the normalized vectors of surface current density J at instant when current density shows a maximum. The white line is representing the 10% isocontour of the maximum value of the surface current density. To maintain the whole frequency band, the results at frequencies 1–6 GHz are shown in Fig. 11(a)–(f). The maximum current surface density is distributed along the
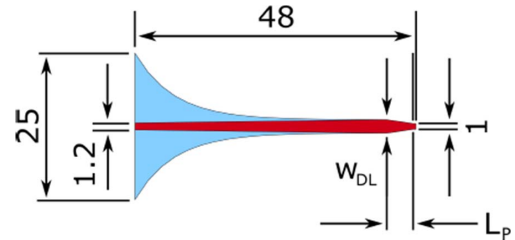

Fig. 9. Final design of the balun shape (dimensions are reported in mm), providing better reflection coefficient with the bowtie arms.
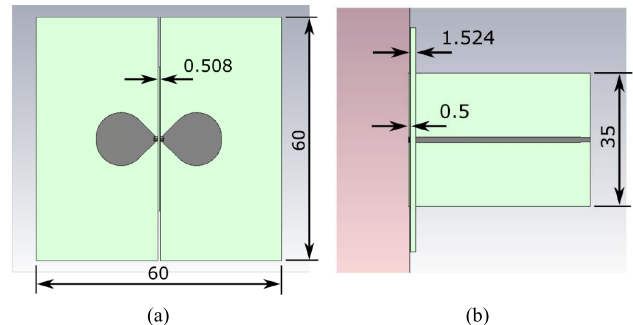

Fig. 10. Finalized geometry of the designed antenna: (a) front view and (b) side view. All dimensions are in millimeters.

edges of the antenna in proximity to the antenna excitation. From Fig. 11(a)–(f), it can be concluded that for all frequencies, the vectors and modules of the surface current density are symmetrical for both arms.
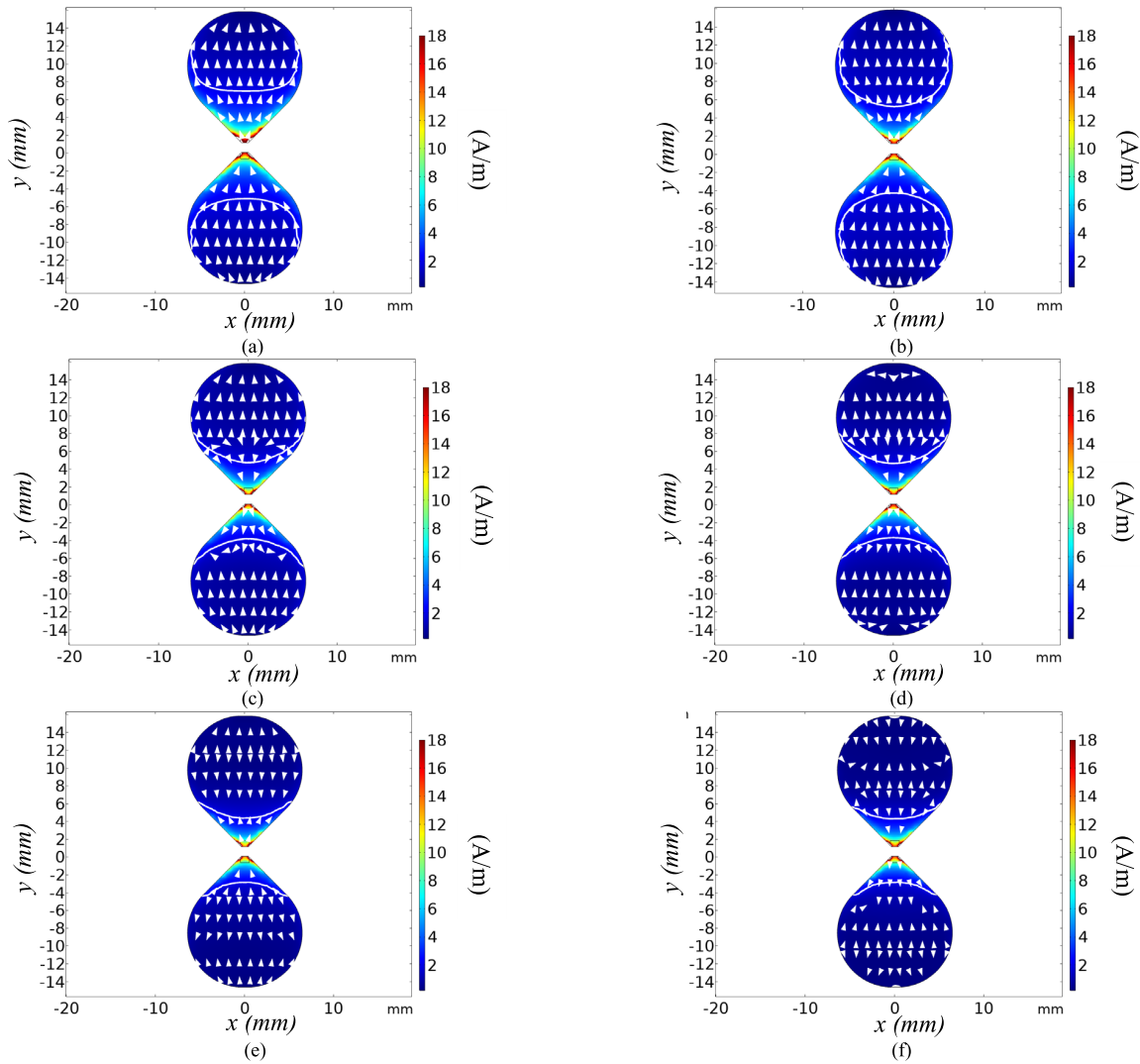
Fig. 11. Surface current density J(A/m) of the antenna at: (a) 1 GHz (b) 2 GHz (c) 3 GHz (d) 4 GHz (e) 5 GHz and (f) 6 GHz in the *xy* plane. The white line represents an isocontour of 10% of the maximum value of the surface current density.

TABLE III
ANTENNA POWER EFFICIENCY CALCULATED ACCORDING TO (1)

	Absorbed power ratio E_f	
	New proposed antenna	Previously used antenna [37]
1 GHz	86.7 %	71.6 %
2 GHz	97.8 %	84.9 %
3 GHz	85.9 %	70.4 %
4 GHz	98.2 %	67.8 %
5 GHz	81.1 %	58.9 %
6 GHz	93.8 %	45.7 %

In Table III the ratio of absorbed power in the brain phantom to input power—parameter E_f at frequencies 1–6 GHz is presented. The data in Table III express how much of the input power is effectively transferred toward the head phantom. The absorbed power consists of power being reflected in the antenna structure due to the impedance mismatch, from power being radiated outside the phantom (backward radiation) and

dissipated in the antenna structure. Based on the described power calculations, the proposed UWB antenna shows ability to deliver above 80% of the input power to the analyzed phantom. The developed UWB antenna delivers on average 20% more energy within the whole frequency bandwidth than our previously used bowtie antenna presented in [37] Instead of the antenna radiation pattern analysis in the far field, we evaluate the antenna radiation based on comparison of normalized magnitudes of the electric field in lossy brain phantom along the antenna radiation angle for different frequencies. The resulted E-field shapes are presented in Fig. 12(a) for E-plane and Fig. 12(b) for H-plane.

Resulted $|S_{11}|$ parameters for antenna being attached to the specific human tissues, such as brain—blue curve, bone—orange curve, skin—violet curve, and muscle—green curve + water—red curve are shown in Fig. 13. According to the results listed in Fig. 13, the antenna, attached to the brain and muscle phantom, is usable to work within the frequency band of 0.5–6 GHz. For the rest of the numerically tested phantoms, the proper working band is limited to 0.5–5 GHz.
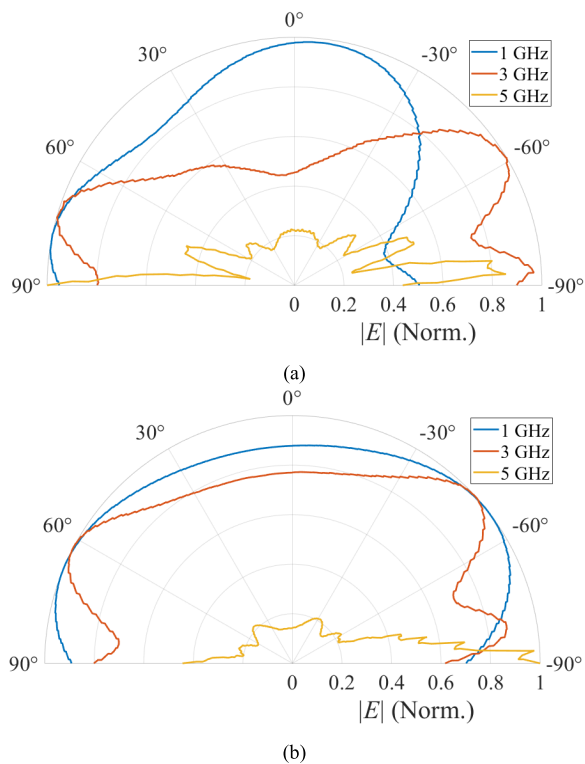
Fig. 12. Normalized magnitudes of the intensity of the electric field $|E|$ dependent on angle for different frequencies: (a) E-plane and (b) H-plane.
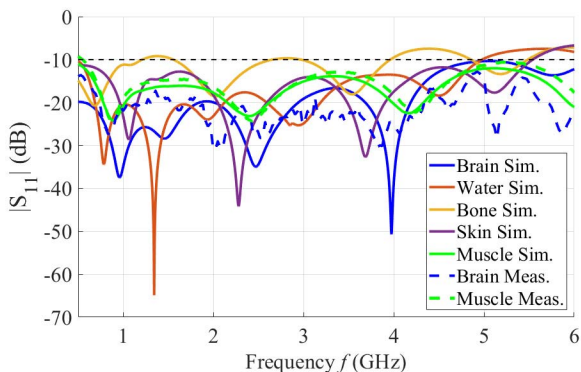

Fig. 13. Comparison of computed magnitudes of reflection coefficients $|S_{11}|$ of proposed antenna attached to a different type of tissues (full lines). Measurements of antenna on brain (blue) and muscle (green) phantom are marked by dashed lines. The level of -10 dB is marked by a black dashed line.
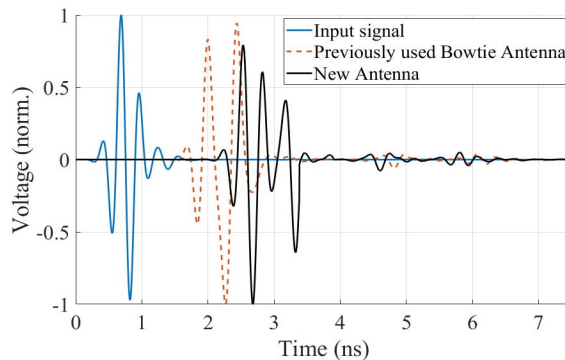

Fig. 14. Comparison of the input signal (blue curve, Gaussian pulse of frequency band of 1–6 GHz) and recorded signals on receiving antenna. Orange dashed line is signal recorded by previously used bowtie antenna and black line is signal recorded by here presented antenna.
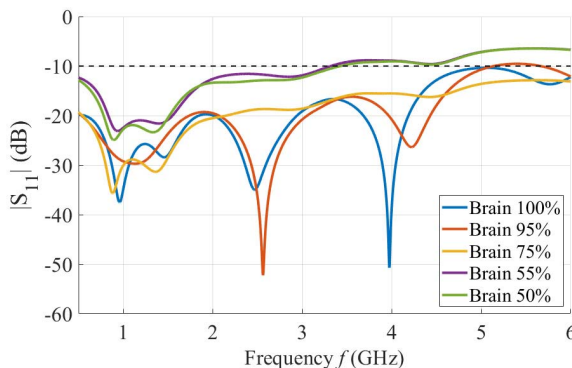

Fig. 15. 15 Comparison of computed magnitudes of reflection coefficients $|S_{11}|$ of proposed antenna for its different contact to the phantom. The percentage is expressing the coverage of the antenna by the brain phantom. The rest is covered by air.
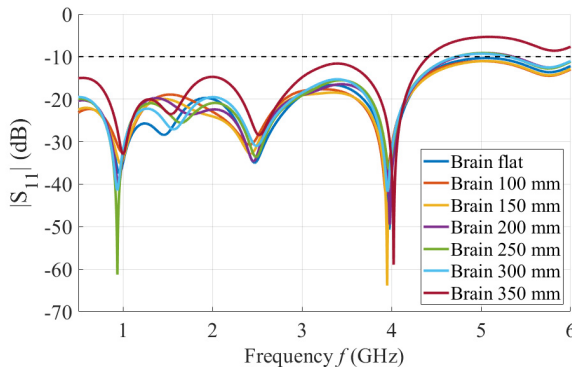

Fig. 16. Comparison of computed magnitudes of reflection coefficients $|S_{11}|$ of proposed antenna attached to the rounded phantom of different radius.

The only exception is bone phantom, where the working frequency band is lower: 0.5–3.8 GHz. The level of -10 dB is visualized by the black dashed line. The -10 dB level indicates the $|S_{11}|$ minimum value where we can assume good antenna functionality. Transmitted and received time domain pulses transferred through brain tissue are presented in Fig. 14. In this numerical study, two identical antennas are placed in opposite each other in distance of 150 mm. Blue curve is the emitted UWB pulse, red dashed curve is UWB pulse received by the previously used bowtie antenna [37], and black curve represents signal received by here presented UWB antenna. Substituting to (2), the calculated fidelity factor F in the brain phantom for the previously used bowtie antenna is

0.86 and for new proposed UWB antenna is 0.81. The fidelity factor of novel antenna is slightly lower than previously used antenna—higher fidelity factor means lower signal distortion. The fidelity factor of the new proposed antenna in case of other tissues as skin and muscle is 0.79 and 0.83, respectively. For bone tissue, the fidelity factor was 0.70. This is corresponding to results of $|S_{11}|$ parameter when the antenna was attached to these tissues (Fig. 14). However, in brain, skin, and muscle, the new antenna shows the ability to transmit and receive the UWB signal without any significant distortion effects and with low subsequent ringing.
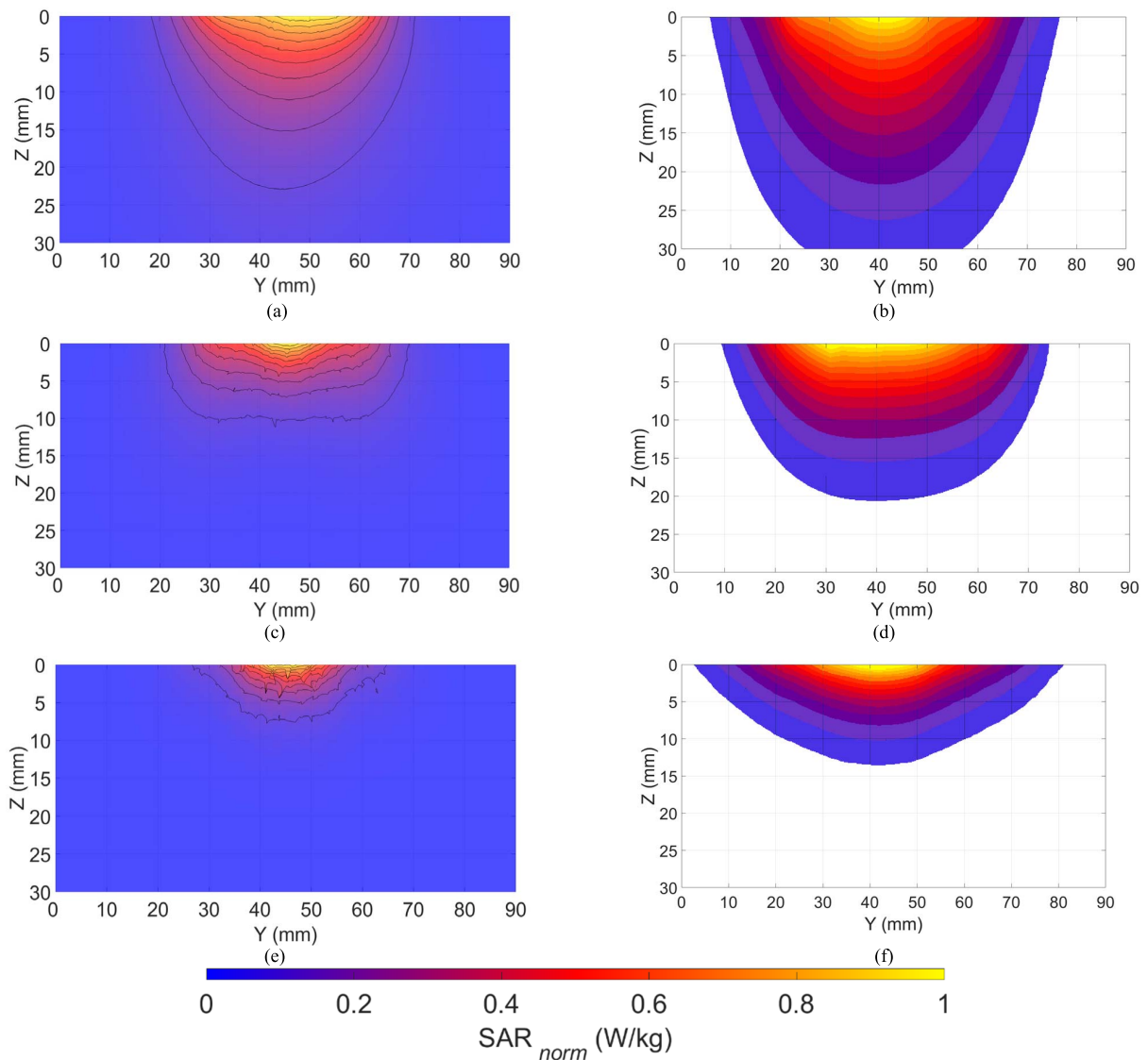
Fig. 17. (a) (c) and (e) Simulated and (b) (d) and (f) measured SAR distributions under proposed UWB antenna in the *yz* plane: (a) and (b) for 2 GHz; (c) and (d) for 4 GHz; and (e) and (f) for 6 GHz.

Fig. 15 shows the values of $|S_{11}|$ parameter when the antenna was attached to the flat phantom with reduced contact from 100% to 50%. For contact 100% (blue curve), 95% (red curve), 75% (yellow curve), the antenna is working in the whole frequency band without any significant changes.

For lower contacts 55% and 50%, the $|S_{11}|$ parameter is under -10 dB within the frequency band of 0.5–3.1 GHz. For antenna contact lower than 55%, the matching liquid is required.

The results in Fig. 16 show the $|S_{11}|$ parameter of the antenna attached to the rounded phantom of different diameters in the range of 100–350 mm. A smaller phantom diameter results in a lower contact between the antenna and the phantom. But for all cases, the central active part with metallic bowties was attached properly. For phantoms of diameter 100–300 mm, the change in the phantom diameter has no significant influence on the $|S_{11}|$ parameter. For higher diameters (350 mm and more), we can expect a reduction of the usable

frequency band and, therefore, the matching liquid will be required. This effect can be caused by the formation of surface waves that propagate at the air–phantom interface.

C. Antenna Measurements Result

The simulation results presented in Fig. 13 were confirmed by a measurement of $|S_{11}|$ parameter on brain and muscle phantom. The real measurements performed using liquid (brain phantom—blue dashed line) and solid phantom (muscle phantom—green dashed line) are indicated by the dashed line.

Fig. 17 shows predicted [Fig. 17(a), (c), and (e)] and measured [Fig. 17(b), (d), and (f)] SAR distributions under the proposed UWB antenna (*yz* plane) in the human brain phantom for frequencies 2, 4, and 6 GHz. The SAR distributions show good homogeneity and symmetry at all discussed frequencies compared with the numerical simulation. The differences between the simulated and measured SAR
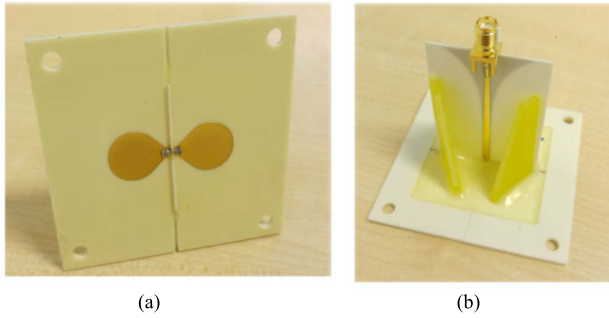
(a)   (b)

Fig. 18.   Photograph of the fabricated antenna element: (a) front view and (b) top view.

distributions are mainly visible in the close proximity of the antenna.

D. Antenna Fabrication

The antenna design is composed of several planar parts, which were fabricated at 1.542 and 0.508 mm (UWB tapered balun) high substrate Rogers RO4003C using the standard PCB technology realized by Pragoboard Ltd., Prague, Czech Republic. The substrate Isola DURAVER (height 2 mm) was used for the mechanical reinforcement of the balun. The mechanical connection was made by standard two component epoxy glue. To the feeding point, the SMA connector was soldered. Photograph of fabricated UWB bowtie antenna is shown in Fig. 18.

III. UWB MICROWAVE HEAD IMAGING SYSTEM

The potential of the proposed UWB bowtie antenna was tested in the MT system developed previously in our laboratory.

A. Methods—MW Brain Imaging System

The MWI system was previously described in [7], including Gauss–Newton MWI reconstruction technique. The system has been modified for an array of eight UWB antennas. This was done with respect to cross-coupling reduction among antennas. The number of used antennas was reduced from 10 to 8 to increase the angle between antennas and thus to reduce the antenna crosstalk. The dimensions of the container are 200×160 mm^2 based on average adult male head [38]. The antennas were equidistantly placed in one ring in the plastic antenna holder to form a multistatic array around the area to be imaged. The whole imaging system is shown in Figs. 19 and 20. The container height is 200 mm height with 2 mm-thick wall. It consists of the octagonal pins at the bottom, which are used for precise phantoms positioning which represents inhomogeneity to be imaged. These cylindrical phantoms have a diameter of 40 mm. All plastic parts of containers were printed using the polyethylene terephthalate glycol (PETG) material at Prusa i3 MK3 (Prusa Research, Czech Prague, Republic) 3-D printer. The antennas were inserted and attached to the wall of container by plastic screws. The mentioned VNA ZNB8-32 connected to the microwave switching matrix ZN-Z84-B42 (Rohde & Schwarz) was used to measure the transmissions between antennas
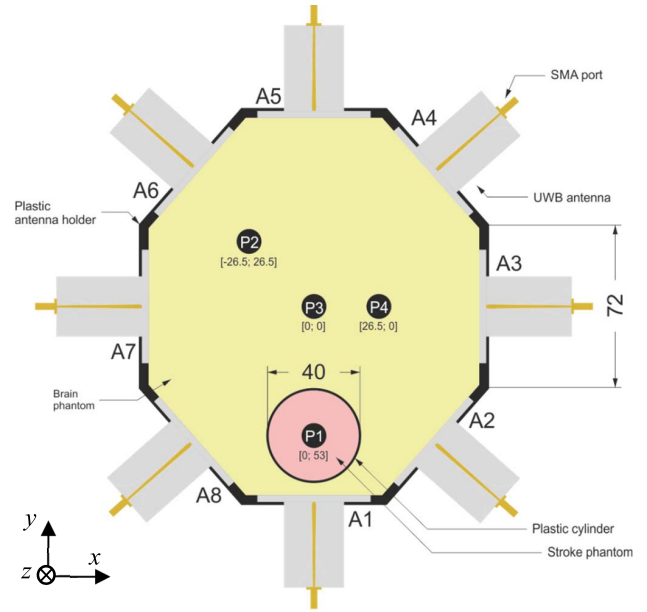

Fig. 19.   Schematic top view of the UWB imaging system with four marked positions of the inhomogeneity phantom P1–P4 (gray: UWB antennas, black: wall of the container, yellow: liquid phantom of human brain, and pink: inhomogeneity phantom).

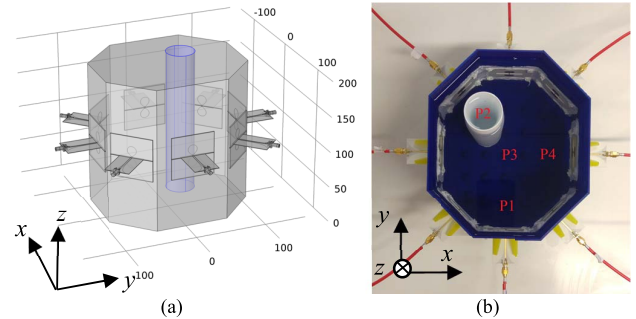(a)   (b)

Fig. 20.   (a) Numerical model used for MT approach of the UWB microwave system (dimensions are in mm) with inserted inhomogeneity phantom (blue); (b) Photograph of the imaging system with UWB antennas connected via switching matrix to the VNA.

(S-parameter matrix). UWB bowtie antennas were connected to the switching matrix using a semirigid coaxial cable.

1) Liquid Phantoms: A liquid phantoms were used for all measurements since they enable to attach the antenna without any air gaps and allow us to place desired inhomogeneity to a predefined position. We prepared phantom with the dielectric parameters of average human brain according to the dielectric properties taken from [29]. The phantom was prepared by mixing of deionized water and isopropyl alcohol. By changing the isopropyl alcohol and deionized water ratio, an additional phantom was prepared, representing a small deviation in dielectric parameters (change in phantom relative permittivity ε_r was approximately +5%). The dielectric parameters of mixed liquid phantom samples were measured using commercial system SPEAG DAK-12 (Schmidt & Partner Engineering AG) at the frequency range of 0.2–3 GHz just before measurements by the MW imaging system. The dielectric probe was connected via coaxial cable to the handheld VNA Fieldfox N9913A (Keysight, Santa Rosa, CA, USA). Measured data were analyzed using SPEAG software to calculate the dielectric properties. The final phantom

TABLE IV

PHANTOMS COMPOSITION AS WEIGHT PERCENTAGE

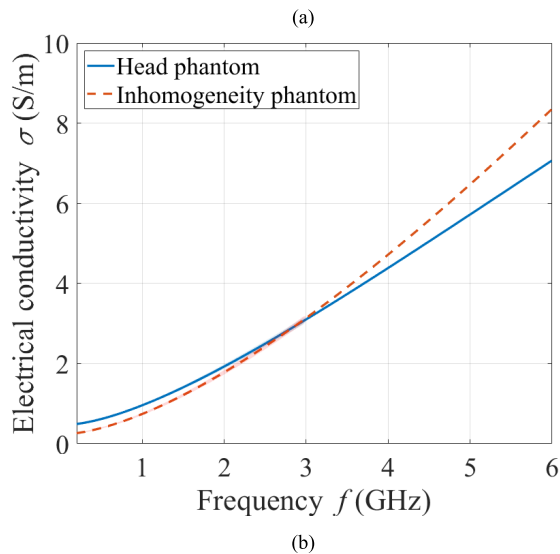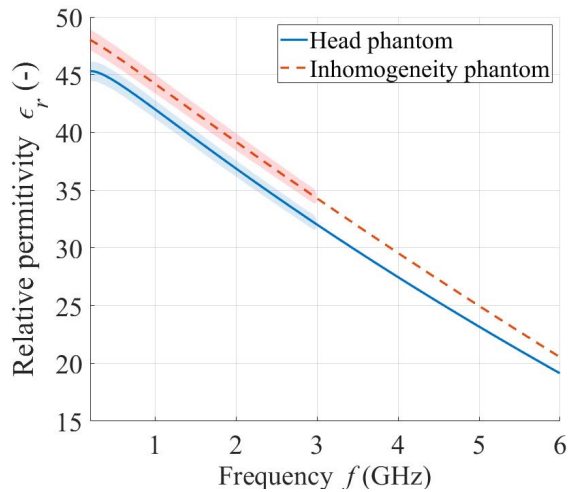| Phantom version	Brain phantom	Inhomogeneity Phantom
Isopropyl Alcohol (wt%)	51.81	45.10
Deionized water (wt%)	47.08	53.81
NaCl (wt%)	1.11	1.09

(a)

(b)

Fig. 21. Cole–Cole model interpolating the measured dielectric properties of phantoms used for antenna testing: (a) relative permittivity and (b) electrical conductivity. The Cole–Cole model extrapolates the values of the dielectric properties of phantoms for higher considered frequencies. Values up to 3 GHz are supplemented by a confidence interval corresponding to the extended measurement uncertainty.

composition is listed in Table IV. The Cole–Cole model was fitted to that measured data by using Levenberg–Marquardt algorithm, where the initial values were set from [29]. The whole procedure is further described in [39]. Dielectric parameters were extrapolated to the frequency band of our interest (0.5–6 GHz).

Fig. 21 shows extrapolated dielectric properties and results of fitted Cole–Cole model. Fig. 21(a) shows relative permittiv-

ity and Fig. 21(b) shows electrical conductivity of the prepared liquid phantoms. Blue curve corresponds to the phantom of human head, and the red curve is presenting the phantom with approximately 5% change in dielectric parameters. This modified phantom was used as an inhomogeneity inserted into the head phantom during simulation and measurement sessions of the imaging system.

Each curve is representing the mean value calculated from ten measurements, while the shading error bars (within the measured frequency band of 0.2–3 GHz) are representing the $\pm$ combined standard uncertainty type C. The composition of each phantom component in weight percent is listed in Table IV.

2) Measurement Procedure—MWI System: The container of MWI system was filled with described liquid brain phantom [Fig. 20(b)]. The plastic cylinder filled with inhomogeneity phantom, representing the inhomogeneity, was inserted in predefined position in container. The whole system is shown in Figs. 19 and 20. Four positions of this cylinder were measured to demonstrate the ability of the MWI system to reconstruct 2-D scattering phantom profile, respectively, and the ability to detect inhomogeneity within the analyzed region. The following measurement parameters were set: frequency bandwidth of 1–6 GHz, VNA output power of 13 dBm, and intermediate frequency bandwidth of 100 Hz.

Following our previous experiences, we neglect frequencies above 6 GHz, which are significantly attenuated in the lossy materials as human brain and thus they do not provide useful information for image reconstruction. All antennas were used in transmit/received mode in which we systematically changed the transmitting single antenna, while all other antennas were set to receive mode. We measured the two scenarios: 1) container filled fully with brain phantom and 2) container filled with brain phantom with inserted inhomogeneity phantom at desired place. This ensured that all scattered and reflected signals were caused just by the inhomogeneity phantom in the cylinder—clutter and background signals were removed. The plastic container for inhomogeneity phantom was present during all measurements. During the measurement, 1) the inhomogeneity container was filled by brain phantom and 2) during the measurement, the inhomogeneity container was filled by inhomogeneity phantom.

3) Signal Processing and Image Reconstruction:

a) Radar approach: The resulting frequency domain data were transformed into the time domain using inverse discrete Fourier transform (IDFT). Thus, the system impulse response matrix was obtained. Time shift $T(d_m)$ for each captured signal and each focal point r_0 was calculated by estimating propagation speed v_p of the EM wave in measured tissue with dielectric constant ε_r and from known round-trip distance d_m of transmitting antenna, of particular, investigated focal point and receiving antenna [2]

$$T(d_m) = \frac{d_m}{v_p}, \quad v_p = \frac{c}{\sqrt{\varepsilon_r(f)}} \tag{3}$$

where c (m/s) is speed of light and ε_r is a relative permittivity of phantom at central frequency of measured bandwidth.

The "Delay and Sum" algorithm was used for the inhomogeneity position reconstruction. By applying this procedure,

2-D energy profile showing scattering/reflecting areas was created. The intensity $I(r_0)$ in particular focal point r_0 was obtained through the following formula:

$$I(r_0) = \left(\sum_{t=-\frac{T_w}{2}}^{\frac{T_w}{2}} \sum_{m=1}^{\frac{N(N+1)}{2}} (w_m(d_m) \cdot \Delta x_m(t + T(d_m)))^2 \right) \quad (4)$$

where T_w is a predefined time-window and w_m is a weighting factor for path dependent attenuation, t is time, N is number of channels, and Δx_m is a differential signal calculated as

$$\Delta x_m(t) = |s_i(t)| - |s_w(t)| \quad (5)$$

where s_i is a signal measured when the inhomogeneity phantom was present, and s_w is a signal measured without inhomogeneity phantom. The signals captured on the antennas with an internal angle wider than 90° to the transmitting antenna have been omitted as they usually do not improve the final image quality [40].

b) MT approach: To demonstrate MT approach, we implemented differential MT algorithm presented by Scapaticci *et al.* [41] and used by Tesarik *et al.* [42] for noninvasive microwave thermometry. This algorithm exploits Born approximation (BA) with regularization by truncated singular value decomposition (TSVD) to reconstruct differential dielectric profile of brain phantom with inhomogeneity placed inside. According to traditional volume integral equation (VIE) defined e.g. in [43] a total electric field of a multiview-multistatic system is equal to the sum of an initial electric field generated by antennae of the system and scattered electric field from objects placed inside the system. The initial EM field was computed by a solution of forward problem using COMSOL Multiphysics (FEM). The model in COMSOL is presented in Fig. 20(a)

Then the VIE can be modified [43], [44] to linear equation

$$\Delta S = \mathbf{L}_e \cdot \Delta O \quad (6)$$

where ΔS is the differential S-matrix calculated as difference between measured S-matrix without any inhomogeneity inside the system and S-matrix with inhomogeneity inside the system. $\mathbf{L}_e$ is a so-called linear operator built from computed electric fields by the forward solver and ΔO ($\Delta \varepsilon_r \Delta \sigma$) is unknown differential object function. TSVD solves (6) where the number of pixels of ΔO is usually larger than the number of independent values of ΔS.

c) Hybrid approach: The combination of radar and MT approach can optimize the process of image reconstruction in terms of speed and accuracy. We can split the process into two steps. First, from the results obtained from the radar-based approach, the algorithm identifies the ROI where the inhomogeneity inside the system is placed. Second, this *a priori* information can be used as input for forward solver or algorithm during MT image reconstruction process, respectively.

Complex permittivity reconstruction using differential MT approach with BA and TSVD regularization is sensitive on artifacts in the resulting image. Usually one or more false reconstructed "hot spots" can be observed. Therefore, the real position of inhomogeneity could be difficult to identify and also lower number of truncation level needs to be applied.

It results to distortion of reconstructed values of differential dielectric parameters.

Using the information about ROI obtained from radar-based approach, the MT reconstruction process is made only in that ROI allows to use higher values of truncation number and thus improves the reconstructed values of differential relative permittivity as well as conductivity. The reconstruction algorithm is also speed up because of using computed initial electric fields only from ROI, thus reducing the size of $\mathbf{L}_e$ and ΔO.

Considering the iterative MT reconstruction algorithms as Gauss–Newton with Tikhonov regularization presented, for instance, in [7], the hybrid approach offers rapid time reduction of estimation of dielectric parameters. To find the values of complex permittivity inside the eight-port MT system using eight iterations took approximately 20 h. Commonly in each interaction, the whole forward numerical model must be solved. If model is limited to exact ROI defined by radar approach, the solution time and image reconstruction by MT approach are shortened.

B. Reconstruction Results—MW Brain Imaging System

1) Radar Approach: Four different inhomogeneity phantom positions (P_1–P_4) were measured as it is shown in Fig. 19. The 2D reconstructed images of four scattering profiles, shown in Fig. 22, were obtained by differential signal processing of the measured impulses (radar method). The position of the inhomogeneity phantom within the container is in each case marked by the red circle. The reconstructed images are presented for clarity by isocontours. The results are showing that by radar method we are able to detect the position of the phantom with 5% change (approximately $+2.5$ in ε_r) in dielectric parameters. For all four positions the maximum intensity is detected within the red circle which is indicating the actual phantom position. It took 90 s to measure and 22 s to reconstruct one inhomogeneity position. For two inhomogeneity positions P_1 and P_2, we detect our ROI marked by pink rectangle in Fig. 22. These ROI were determined as double distance between the isocontour 0.9 and 0.5 to all directions.

2) Hybrid Approach: The measured representative $|S_{nn}|$ and $|S_{mn}|$ parameters for case when the inhomogeneity was placed in position P_4 (according to Fig. 19) are presented in Fig. 23. The blue curve is representing the $|S_{33}|$ parameter (in that case, antenna 3 is the nearest antenna to the inhomogeneity position P_4). The blue shading error bar is representing the standard deviation of all $|S_{nn}|$ parameters—of all antennas in the system (A1–A8). The representative transmission coefficients are presented by red ($|S_{32}|$), orange ($|S_{34}|$) and violet ($|S_{37}|$) curve. The lowest transmission coefficients are identical for all here presented signals (between 3.5 and 5 GHz), where the transmission coefficients reach values around -90 dB. At the frequency around 4 GHz the $|S_{37}|$ exceeds the value -100 dB. Absolute value of differential transmission coefficients $|\Delta S_{mn}|$ between the cases with inhomogeneity (inhomogeneity position P_4) and without inhomogeneity is shown in Fig. 24. Based on ROI's defined by radar approach around positions of inhomogeneity P_1 and P_2, we reconstructed the differential
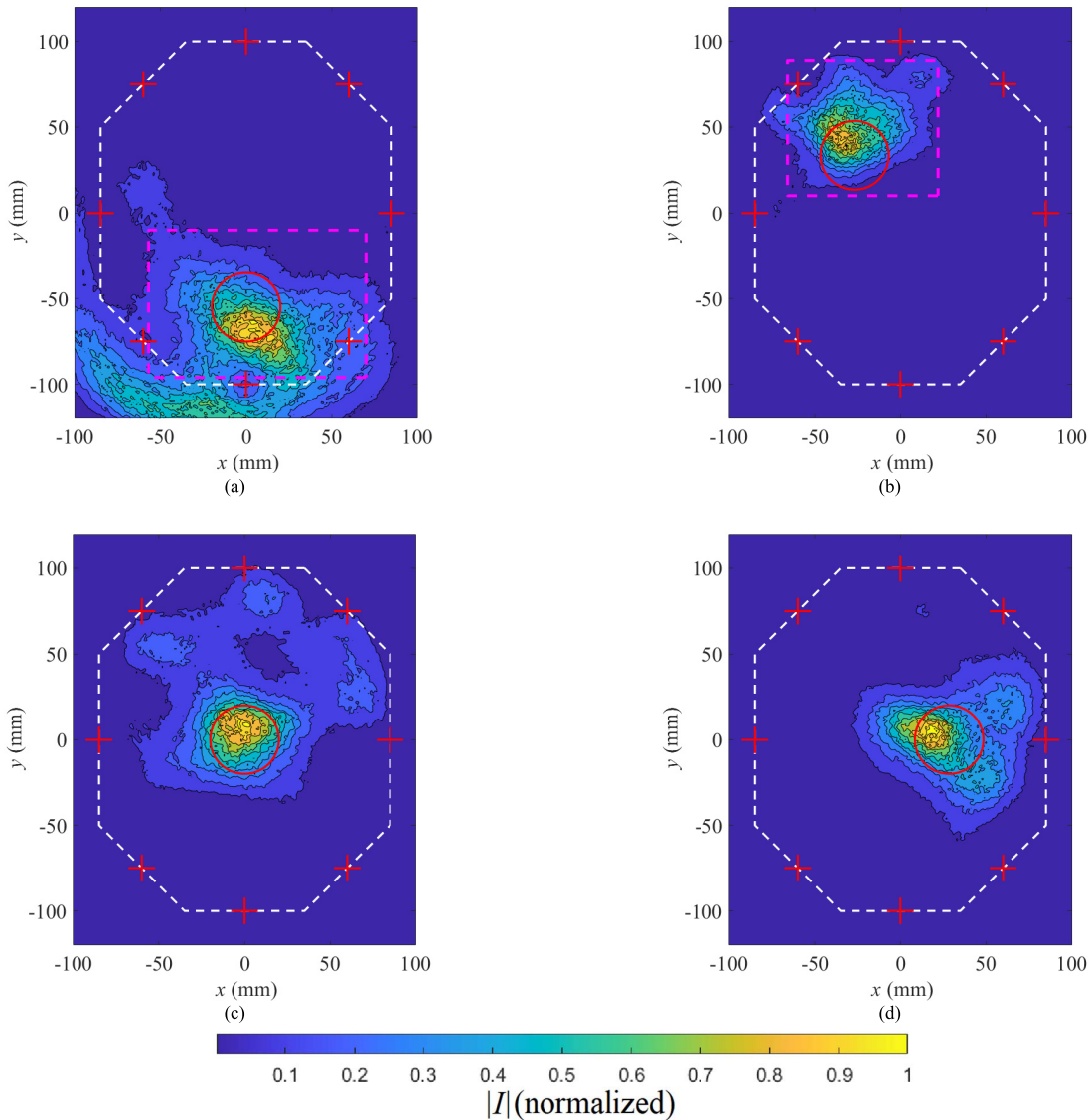
Fig. 22. Reconstructed scattering profile (normalized intensity $|I|$) of liquid brain phantom with inserted cylindrical-shaped dielectric inhomogeneity. The position (P_1–P_4) of the inhomogeneity is marked by the red circle. (a) Correspoding to the inhomogeneity position P_1. (b) Position P_2. (c) Position P_3. (d) Position P_4. The antennas positions are marked by red crosses. The inner container boards are marked by the white line.
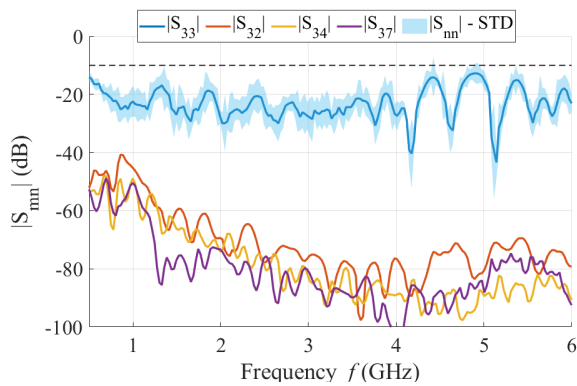

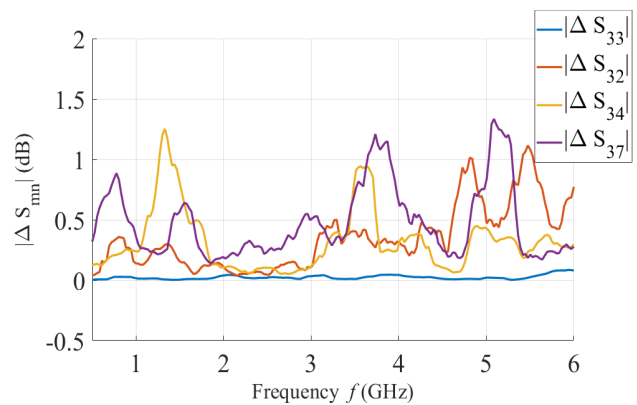Fig. 23. Representative transmission coefficients for the inhomogeneity position P_4.

Fig. 24. $|\Delta S_{mn}|$ transmission coefficients between the cases with inhomogeneity (position P4) and without inhomogeneity.

relative permittivity as well as electrical conductivity profiles inside the ROI's using MT approach. We used the operation frequency of 1 GHz as reasonable frequency regarding the

space resolution and penetration depth of EM wave. The truncation level of TSVD was set to 28 where the maximal value is equal to 36. The reconstructed images are depicted
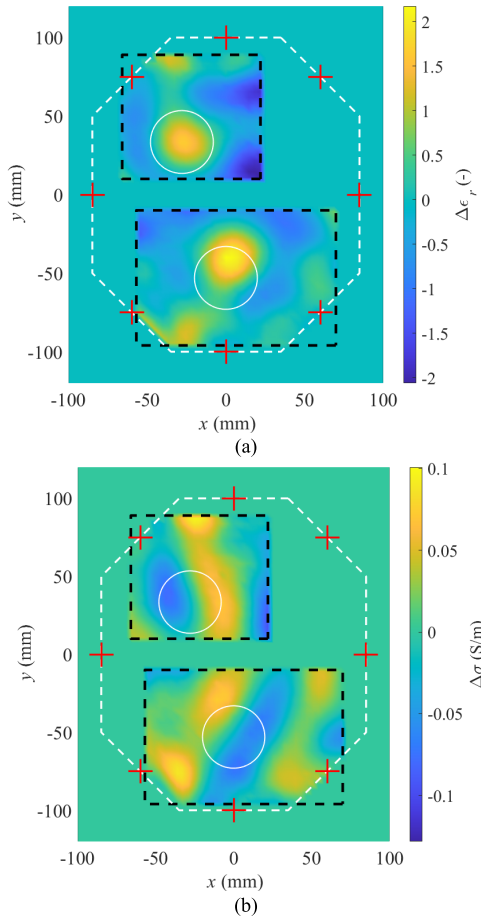
Fig. 25. Reconstructed differential dielectric profile: (a) relative permittivity and (b) electrical conductivity of liquid brain phantom with inserted cylindrical inhomogeneity. The true position of the inhomogeneity P_1 and P_2 is marked by the white circle. The antennas positions are marked by red crosses. The inner surfaces of the container walls are marked with a white dashed line.

in Fig. 25. We can see that both positions of inhomogeneity were correctly identified by MT algorithm based on differential relative permittivity data. The reconstructed contrast of differential relative permittivity approximately $+2$ especially in P_1 ROI was in very good match with measured value $+1.56$ by commercial dielectric probe. In the image also the artifact of negative differential contrast -2 was reconstructed and is visible in the right down corner of P_1 ROI.

Due to radar-based ROI identification this artifact was eliminated, and true position and contrast of inhomogeneity were determined. The reconstructed differential electrical conductivity data were distorted and neither the data limitation by ROI helped to get satisfying results.

IV. DISCUSSION

The UWB bowtie antenna for application in UWB MWI systems was designed and its calculated characteristics confirmed by series of numerical simulations and measurements. Bowtie arms were miniaturized by edge rounding which is beneficial in MWI systems with higher number of antennas. Smaller dipole arms dimensions have a positive influence on the antenna impulse response. We designed the UWB balun which provides sufficient reflection coefficient

($|S_{11}| < -10$ dB) in its entire frequency band (1–6 GHz) when connected to the bowtie dipole arms. Here, the presented UWB antenna stands out above the other UWB antennas designed for MWI [23]–[28] especially in the wide usable frequency bandwidth (1–6 GHz) which provides sufficient resolution for most biomedical application of MWI. The comparable antennas intended for MWI are listed in Table I with their basic parameters. To prove this statement, the final antenna element was attached to various types of tissues and the $|S_{11}|$ parameter was simulated. The simulation results show that the antenna is fully functional ($|S_{11}| < -10$ dB) in its entire frequency band (1–6 GHz) for tissues that have higher water content (brain and muscle). For skin tissue, the frequency band decreased slightly to 1–5 GHz. For tissues (bone tissue in our case) with low water content, we believe that the frequency band is still useful between 1 and 4 GHz. The predicted UWB bowtie antenna $|S_{11}|$ characteristic was confirmed by measurement by using muscle and brain phantom (within the imaging system) in the 1–6 GHz frequency band with magnitude well below -12 dB in the whole studied frequency band.

The fractional bandwidth of our antenna is 143%. The fractional bandwidth (and subsequently applicable frequency bandwidth) is one of the highest values which can be found in the literature. This ensures short impulse response of the antenna. Only the antenna presented in [28] is offering higher fractional bandwidth (163%) with comparable fidelity factor and is designed for the head imaging. Our UWB antenna possesses a high radiation efficiency (over 80% in the whole frequency band) to the brain phantom and, therefore, does not suffer from high backward radiation. The antennas with high effectivity are able to transmit higher energy and thus detect lower dielectric changes. Simulated and measured SAR distributions as well as $|E|$ field distribution in the brain phantom of the proposed antenna shown symmetrical radiation pattern. Final antenna dimensions are $60 \times 60 \times 50$ mm^3. The front panel of dimensions 60×60 mm^2 was chosen as appropriate for insertion to the brain imaging system previously developed in our laboratory. However, the simulation of the antenna sensitivity to air gaps between antenna and brain phantom showed that in the presence of air under active part (metallic bowties), the antenna performance is low and, therefore, application of matching liquid is required. If the air gap is outside the antenna active area, that air gap has no or very low effect on $|S_{11}|$. The fidelity factor for brain phantom was 0.81, for skin 0.79, and for muscle 0.83. In case of bone tissue, the fidelity was lower (0.70). According to our experience, the fidelity factor around 0.80 is perfectly sufficient for MWI techniques and offers adequate spatial resolution. Due to the large UWB bandwidth, the fidelity factor is lower compared with the antennas previously published (fidelity factor in [23]–[28] ranges from 80% to 92%). This ensures that presented antenna has minimal time domain distortion of the Tx/Rx signals.

Developed UWB bowtie antenna was implemented in eight channel microwave UWB imaging system. Results showed very good detectability of the inhomogeneity position within head phantom by the radar approach. The ROI was selected using reconstructed data from the radar approach. This ROI

was used as an input *a priori* information to MT approach based on BA. This led to an increased accuracy of the reconstruction as well as filtering of unwanted hotspots. The reconstruction process was also speeded up by approximately 20% due to reducing the investigation domain only on ROI. The reconstruction of measured data based on electrical conductivity profile was distorted and not fully successful. It could be caused by too high truncation level. Since the conductivity changes were in orders of tenths, the stability of the algorithm could be oversaturated. Reduction of truncation level would lead to decrease of reconstructed contrast accuracy of relative permittivity data. Increasing the antennas number and its positions in different rings can lead to better reconstruction accuracy. The scattering profile reconstruction shows that also for very low change in dielectric parameters enabling the system to accurately detect the stroke position.

V. Conclusion

In this work, the design of an UWB antenna for MWI was presented, and its suitability was experimentally verified. The presented UWB antenna shows a high radiation efficiency (above 80%) and a symmetrical radiation pattern in the whole working frequency band. The useful frequency band is very wide (1–6 GHz) which allows the antenna to be used for most MWI applications offering high spatial resolution. The fidelity factor over 80% ensures good antenna functionality with low distortion and good impulse response. The antenna parameters, such as good $|S_{11}|$, working frequency band, and radiation efficiency, are important for the sensitivity of the reconstruction algorithms. Our antenna has fulfilled all parameters mentioned above in the whole UWB band. The compactness of the antenna predestines it for MWI systems with a higher number of antenna elements, and the construction of the antenna then enables cheap and repeatable production by established methods of production of printed circuit boards. The antenna can thus be used as the basis for more accurate MWI multifrequency systems and can also be implemented in UWB MWI hybrid systems combining MT and radar approaches.

References

[1] M. T. Islam, M. Z. Mahmud, M. T. Islam, S. Kibria, and M. Samsuzzaman, "A low cost and portable microwave imaging system for breast tumor detection using UWB directional antenna array," *Sci. Rep.*, vol. 9, no. 1, pp. 1–13, Dec. 2019, doi: 10.1038/s41598-019-51620-z.

[2] R. C. Conceição, J. J. Mohr, and M. O'Halloran, Eds., *An Introduction to Microwave Imaging for Breast Cancer Detection*. Cham, Switzerland: Springer, 2016.

[3] S. Noghanian, A. Sabouni, T. Desell, and A. Ashtari, *Microwave Tomography: Global Optimization, Parallelization and Performance Evaluation*. New York, NY, USA: Springer, 2014.

[4] O. Fiser, M. Helbig, J. Sachs, S. Ley, I. Merunka, and J. Vrba, "Microwave non-invasive temperature monitoring using UWB radar for cancer treatment by hyperthermia," *Prog. Electromagn. Res.*, vol. 162, pp. 1–14, 2018, doi: 10.2528/pier17111609.

[5] T. M. Grzegorczyk, P. M. Meaney, P. A. Kaufman, R. M. di Florio-Alexander, and K. D. Paulsen, "Fast 3-D tomographic microwave imaging for breast cancer detection," *IEEE Trans. Med. Imag.*, vol. 31, no. 8, pp. 1584–1592, Aug. 2012, doi: 10.1109/TMI.2012.2197218.

[6] J. A. Tobon Vasquez *et al.*, "A prototype microwave system for 3D brain stroke imaging," *Sensors*, vol. 20, no. 9, p. 2607, May 2020, doi: 10.3390/S20092607.

[7] I. Merunka, A. Massa, D. Vrba, O. Fiser, M. Salucci, and J. Vrba, "Microwave tomography system for methodical testing of human brain stroke detection approaches," *Int. J. Antennas Propag.*, vol. 2019, Mar. 2019, Art. no. 4074862, doi: 10.1155/2019/4074862.

[8] Y. A. Rahama, O. Al Aryani, U. A. Din, M. A. Awar, A. Zakaria, and N. Qaddoumi, "Novel microwave tomography system using a phased-array antenna," *IEEE Trans. Microw. Theory Techn.*, vol. 66, no. 11, pp. 5119–5128, Nov. 2018, doi: 10.1109/TMTT.2018.2859929.

[9] C. Dachena, A. Fedeli, A. Fanti, M. B. Lodi, M. Pastorino, and A. Randazzo, "Microwave imaging for the diagnosis of cervical diseases: A feasibility analysis," *IEEE J. Electromagn., RF Microw. Med. Biol.*, vol. 5, no. 3, pp. 277–285, Sep. 2021, doi: 10.1109/JERM.2020.3042711.

[10] B. Amin *et al.*, "A feasibility study on microwave imaging of bone for osteoporosis monitoring," *Med. Biol. Eng. Comput.*, vol. 59, no. 4, pp. 925–936, Apr. 2021, doi: 10.1007/S11517-021-02344-8.

[11] J. Sachs, S. Ley, T. Just, S. Chamaani, and M. Helbig, "Differential ultra-wideband microwave imaging: Principle application challenges," *Sensors*, vol. 18, no. 7, p. 2136, Jul. 2018, doi: 10.3390/s18072136.

[12] E. C. Fear, X. Li, S. C. Hagness, and M. A. Stuchly, "Confocal microwave imaging for breast cancer detection: Localization of tumors in three dimensions," *IEEE Trans. Biomed. Eng.*, vol. 49, no. 8, pp. 812–822, Aug. 2002, doi: 10.1109/TBME.2002.800759.

[13] H. Song *et al.*, "Detectability of breast tumor by a hand-held impulse-radar detector: Performance evaluation and pilot clinical study," *Sci. Rep.*, vol. 7, no. 1, p. 16353, Dec. 2017, doi: 10.1038/s41598-017-16617-6.

[14] A. Baran, D. J. Kurrant, A. Zakaria, E. C. Fear, and J. LoVetri, "Breast imaging using microwave tomography with radar-based tissue-regions estimation," *Prog. Electromagn. Res.*, vol. 149, pp. 161–171, 2014, doi: 10.2528/PIER14080606.

[15] A. Sabouni, D. Flores-Tapia, S. Noghanian, G. Thomas, and S. Pistorius, "Hybrid microwave tomography technique for breast cancer imaging," in *Proc. Int. Conf. IEEE Eng. Med. Biol. Soc.*, Aug. 2006, pp. 4273–4276, doi: 10.1109/IEMBS.2006.260615.

[16] J. Bourqui, M. Okoniewski, and E. C. Fear, "Balanced antipodal Vivaldi antenna with dielectric director for near-field microwave imaging," *IEEE Trans. Antennas Propag.*, vol. 58, no. 7, pp. 2318–2326, Jul. 2010, doi: 10.1109/TAP.2010.2048844.

[17] X. Li, S. C. Hagness, M. K. Choi, and D. W. V. D. Weide, "Numerical and experimental investigation of an ultrawideband ridged pyramidal horn antenna with curved launching plane for pulse radiation," *IEEE Antennas Wireless Propag. Lett.*, vol. 2, pp. 259–262, 2003, doi: 10.1109/LAWP.2003.820708.

[18] F. S. Di Clemente, M. Helbig, J. Sachs, U. Schwarz, R. Stephan, and M. A. Hein, "Permittivity-matched compact ceramic ultra-wideband horn antennas for biomedical diagnostics," in *Proc. 5th Eur. Conf. Antennas Propag. (EUCAP)*, Apr. 2011, pp. 2386–2390.

[19] H. M. Jafari, M. J. Deen, S. Hranilovic, and N. K. Nikolova, "A study of ultrawideband antennas for near-field imaging," *IEEE Trans. Antennas Propag.*, vol. 55, no. 4, pp. 1184–1188, Apr. 2007, doi: 10.1109/TAP.2007.893405.

[20] A. H. M. Z. Alam, M. R. Islam, and S. Khan, "Design and analysis of UWB rectangular patch antenna," in *Proc. Asia–Pacific Conf. Appl. Electromagn.*, Dec. 2007, pp. 1–3, doi: 10.1109/APACE.2007.4603851.

[21] O. Yurduseven, D. Smith, and M. Elsdon, "Printed slot loaded bow-tie antenna with super wideband radiation characteristics for imaging applications," *IEEE Trans. Antennas Propag.*, vol. 61, no. 12, pp. 6206–6210, Dec. 2013, doi: 10.1109/TAP.2013.2281353.

[22] H. Kanj and M. Popović, "Miniaturized microstrip-fed 'dark eyes' antenna for near-field microwave sensing," *IEEE Antennas Wireless Propag. Lett.*, vol. 4, pp. 397–401, 2005, doi: 10.1109/LAWP.2005.859377.

[23] X. Li, M. Jalilvand, Y. L. Sit, and T. Zwick, "A compact double-layer on-body matched Bowtie antenna for medical diagnosis," *IEEE Trans. Antennas Propag.*, vol. 62, no. 4, pp. 1808–1816, Apr. 2014, doi: 10.1109/TAP.2013.2297158.

[24] M. Rokunuzzaman, A. Ahmed, T. C. Baum, and W. S. T. Rowe, "Compact 3-D antenna for medical diagnosis of the human head," *IEEE Trans. Antennas Propag.*, vol. 67, no. 8, pp. 5093–5103, Aug. 2019, doi: 10.1109/TAP.2019.2908066.

[25] A. S. M. Alqadami, N. Nguyen-Trong, B. Mohammed, A. E. Stancombe, M. T. Heitzmann, and A. Abbosh, "Compact unidirectional conformal antenna based on flexible high-permittivity custom-made substrate for wearable wideband electromagnetic head imaging system," *IEEE Trans. Antennas Propag.*, vol. 68, no. 1, pp. 183–194, Jan. 2020, doi: 10.1109/TAP.2019.2938849.

[26] X. Lin, Y. Chen, Z. Gong, B.-C. Seet, L. Huang, and Y. Lu, "Ultraw-ideband textile antenna for wearable microwave medical imaging applications," *IEEE Trans. Antennas Propag.*, vol. 68, no. 6, pp. 4238–4249, Jun. 2020, doi: 10.1109/TAP.2020.2970072.

[27] D. O. Rodriguez-Duarte, J. A. T. Vasquez, R. Scapaticci, L. Crocco, and F. Vipiana, "Brick-shaped antenna module for microwave brain imaging systems," *IEEE Antennas Wireless Propag. Lett.*, vol. 19, no. 12, pp. 2057–2061, Dec. 2020, doi: 10.1109/LAWP.2020.3022161.

[28] M. Ojaroudi, S. Bila, and M. Salimi. (Mar. 2019). *A Novel Approach of Brain Tumor Detection using Miniaturized High-Fidelity UWB Slot Antenna Array.* Accessed: Sep. 13, 2021. [Online]. Available: https://hal-unilim.archives-ouvertes.fr/hal-02377024

[29] P. Hasgall and E. Neufeld. (2017). *IT'IS Database for Thermal and Electromagnetic Parameters of Biological Tissues.* Accessed: Jan. 10, 2021. [Online]. Available: www.itis.ethz.ch/database

[30] S. W. Qu and C. L. Ruan, "Effect of round corners on bowtie antennas," *Prog. Electromagn. Res.*, vol. 57, pp. 179–195, 2006, doi: 10.2528/PIER05072103.

[31] W. Che, L. Gu, and Y. L. Chow, "Formula derivation and verification of characteristic impedance for offset double-sided parallel strip line (DSPSL)," *IEEE Microw. Wireless Compon. Lett.*, vol. 20, no. 6, pp. 304–306, Jun. 2010, doi: 10.1109/LMWC.2010.2047452.

[32] C. A. Balanis, *Antenna Theroy: Analysis and Design.* Hoboken, NJ, USA: Wiley, 2012.

[33] D. M. Pozar, *Microwave Engineering*, 4th ed. Amherst, MA, USA: Wiley, 2012.

[34] cSAR3D Flat. *SPEAG, Schmid & Partner Engineering AG.* Accessed: Sep. 13, 2021. [Online]. Available: https://speag.swiss/products/csar3d/csar3d-systems/csar3d-flat/

[35] H. Kato, M. Hiraoka, and T. Ishida, "An agar phantom for hyperthermia," *Med. Phys.*, vol. 13, no. 3, pp. 396–398, May 1986, doi: 10.1118/1.595882.

[36] G. Quintero, J. F. Zurcher, and A. K. Skrivervik, "System fidelity factor: A new method for comparing UWB antennas," *IEEE Trans. Antennas Propag.*, vol. 59, no. 4, pp. 2502–2512, Jul. 2011, doi: 10.1109/TAP.2011.2152322.

[37] I. Merunka, D. Vrba, O. Fiser, J. Cumana, and J. Vrba, "2D microwave system for testing of brain stroke imaging algorithms," in *Proc. Eur. Microw. Conf. Central Eur. (EuMCE)*, May 2019, pp. 508–511.

[38] K. M. Bushby, T. Cole, J. N. Matthews, and J. A. Goodship, "Centiles for adult head circumference," *Arch. Disease Childhood*, vol. 67, no. 10, pp. 1286–1287, 1992, doi: 10.1136/adc.67.10.1286.

[39] S. Ley, S. Schilling, O. Fiser, J. Vrba, J. Sachs, and M. Helbig, "Ultrawideband temperature dependent dielectric spectroscopy of porcine tissue and blood in the microwave frequency range," *Sensors*, vol. 19, no. 7, p. 1707, Apr. 2019, doi: 10.3390/s19071707.

[40] M. Helbig, M. Kmec, J. Sachs, C. Geyer, I. Hilger, and G. Rimkus, "Aspects of antenna array configuration for UWB breast imaging," in *Proc. 6th Eur. Conf. Antennas Propag. (EUCAP)*, Mar. 2012, pp. 1737–1741, doi: 10.1109/EuCAP.2012.6206594.

[41] R. Scapaticci, O. M. Bucci, I. Catapano, and L. Crocco, "Differential microwave imaging for brain stroke followup," *Int. J. Antennas Propag.*, vol. 2014, Jan. 2014, Art. no. 312528, doi: 10.1155/2014/312528.

[42] J. Tesarik, J. Vrba, and H. D. Trefna, "Non-invasive thermometry during hyperthermia using differential microwave imaging approach," in *Proc. 15th Eur. Conf. Antennas Propag. (EuCAP)*, Mar. 2021, doi: 10.23919/EUCAP51087.2021.9411253.

[43] M. Haynes, J. Stang, and M. Moghaddam, "Microwave breast imaging system prototype with integrated numerical characterization," *Int. J. Biomed. Imag.*, vol. 2012, pp. 1–18, Jan. 2012, doi: 10.1155/2012/706365.

[44] M. Haynes, J. Stang, and M. Moghaddam, "Real-time microwave imaging of differential temperature for thermal therapy monitoring," *IEEE Trans. Biomed. Eng.*, vol. 61, no. 6, pp. 1787–1797, Jun. 2014, doi: 10.1109/TBME.2014.2307072.

Vojtech Hruby received the M.S. degree in radio and optical technology from Czech Technical University (CTU) in Prague, Prague, Czech Republic, in 2019.

He currently works as an Research and Development Engineer with CTS Corporation, Prague facility, Nupaky, Czech Republic.

Jan Vrba (Life Member, IEEE) received the M.Sc. and Ph.D. degrees from Czech Technical University (CTU) in Prague, Prague, Czech Republic, in 1972 and 1976, respectively.

Since 1993, he has been a Full Professor of Radioelectronics with the Department of Electromagnetic Field, CTU in Prague.

Tomas Drizdal received the M.Sc. and Ph.D. degrees from Czech Technical University (CTU) in Prague, Prague, Czech Republic, in 2005 and 2010, respectively.

He is currently working with the Department of Biomedical Technology, CTU in Prague.

Jan Tesarik received the M.Sc. degree in biomedical engineering from Czech Technical University (CTU) in Prague, Prague, Czech Republic, in 2016, where he is currently pursuing the Ph.D. degree.

Jan Vrba, Jr. received the M.Sc. and Ph.D. degrees in electrical engineering from RWTH Aachen University, Aachen, Germany, in 2006 and 2013, respectively.

He is currently working as a Full Professor with Czech Technical University (CTU) in Prague, Prague, Czech Republic.

Ondrej Fiser (Member, IEEE) received the M.Sc. and Ph.D. degrees in electrical engineering from Czech Technical University (CTU) in Prague, Prague, Czech Republic, in 2013 and 2018, respectively.

He is currently working with the Faculty of Biomedical Engineering, CTU in Prague.

David Vrba (Member, IEEE) received the M.Sc. and Ph.D. degrees in electrical engineering from Czech Technical University (CTU) in Prague, Prague, Czech Republic, in 2008 and 2012, respectively.

He has been an Associate Professor with the Faculty of Biomedical Engineering, CTU in Prague, since 2018.